

Nanometer-scale anatomy of entire Stardust tracks

Keiko NAKAMURA-MESSENGER^{1,2*}, Lindsay P. KELLER¹, Simon J. CLEMETT^{1,3},
Scott MESSENGER¹, and Motoo ITO^{1,4,5}

¹Robert M. Walker Laboratory for Space Science, Astromaterials Research and Exploration Science Directorate,
NASA Johnson Space Center, Houston, Texas 77058, USA

²ESCG/Jacobs Technology, Houston, Texas 77058, USA

³ESCG/ERC Inc., Houston, Texas 77058, USA

⁴Lunar and Planetary Institute, Houston, Texas 77058, USA

⁵Present address: Kochi Institute for Core Sample Research, JAMSTEC, Kochi 783-8502, Japan

*Corresponding author. E-mail: keiko.nakamura-1@nasa.gov

(Received 26 September 2010; revision accepted 19 April 2011)

Abstract—We have developed new sample preparation and analytical techniques tailored for entire aerogel tracks of Wild 2 sample analyses both on “carrot” and “bulbous” tracks. We have successfully ultramicrotomed an entire track along its axis while preserving its original shape. This innovation allowed us to examine the distribution of fragments along the entire track from the entrance hole all the way to the terminal particle. The crystalline silicates we measured have Mg-rich compositions and O isotopic compositions in the range of meteoritic materials, implying that they originated in the inner solar system. The terminal particle of the carrot track is a ¹⁶O-rich forsteritic grain that may have formed in a similar environment as Ca-, Al-rich inclusions and amoeboid olivine aggregates in primitive carbonaceous chondrites. The track also contains submicron-sized diamond grains likely formed in the solar system. Complex aromatic hydrocarbons distributed along aerogel tracks and in terminal particles. These organics are likely cometary but affected by shock heating.

INTRODUCTION

The Stardust spacecraft captured dust samples from comet 81P/Wild 2 at impact velocity of 6.1 km s⁻¹ in a low-density silica aerogel and returned them to the Earth (Brownlee et al. 2006). The laboratory analysis of these cometary materials has opened a new window into understanding one of the least understood, but most important types of solar system material. Comets formed in the most distant, cold, and quiescent parts of the solar system, and consequently they have long been considered to harbor the best preserved remnants of the original building blocks of the solar system. By some estimates, cometary ices accreted at temperatures near absolute zero (< 30 K), leading to speculation they could be composed of essentially pristine aggregates of presolar materials (Bockelée-Morvan et al. 2004). The examination of comet 81P/Wild 2 (hereafter Wild 2) samples has allowed some of these ideas to be directly tested in the laboratory

for the first time. Wild 2 samples have already provided many surprises, including: the discovery of refractory minerals (Zolensky et al. 2006), the presence of chondrule-like objects (Nakamura et al. 2008, 2009), and surprisingly low abundances of presolar grains (McKeegan et al. 2006) and indigenous organic materials (Sandford et al. 2006; Keller et al. 2006; Clemett et al. 2010). It is also uncertain whether or not Stardust samples contain the abundant amorphous silicates, so called GEMS (glass with embedded metal and sulfides) grains (Bradley 1994; Keller and Messenger 2011). GEMS grains are major components of chondritic-porous interplanetary dust particles (CP-IDPs) which are thought to also be derived from comets (Ishii et al. 2008). These observations have prompted suggestions that Wild 2 may be comprised largely of altered materials and so is more similar to carbonaceous chondrites than the prevailing view of comets as primitive unaltered bodies (Ishii et al. 2008). While some of these observations can

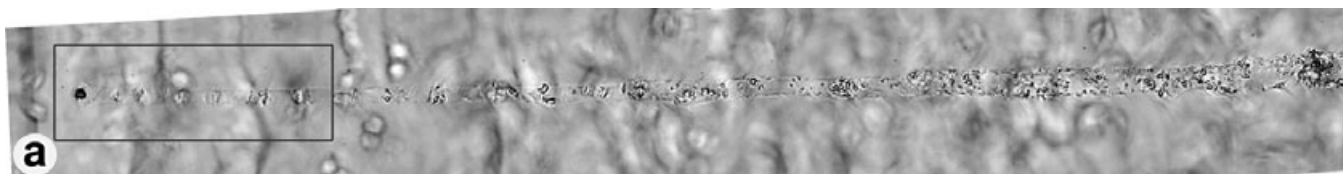


Fig. 1. T112 1947 μm long carrot type track. a) Extended depth of field optical micrograph of T112 prior to analysis. Maximum diameter is 53 μm . High-contrast objects along the track include cometary material and compressed melt aerogel mixed with cometary material. Red arrow indicates a boulder object on the track wall detailed in Fig. 7d. b) Magnified view of the boxed area in (a) before the terminal particle extraction. c) Magnified view of the boxed area in (a) after the terminal particle extraction. Note that damage to the rest of the track from the terminal particle extraction is minimal. d) High magnification optical micrograph of the extracted terminal particle of T112 (6 μm in diameter).

be attributed to sample capture effects, the nature of samples collected from Wild 2 clearly indicates that the origin and evolution of comets are more involved and complex than previously suspected.

The state of Wild 2 samples poses a major challenge to their study. The samples are diverse, they are intimately mixed with aerogel (Keller et al. 2006; Zolensky et al. 2006), and have experienced varying degrees of shock-induced thermal alteration (Tomeoka et al. 2008). The morphology of aerogel tracks indicates different structural and compositional properties of the impactors (Hörz et al. 2006). Carrot (type A) tracks, having slender tapering walls, are thought to have been produced by compact aggregates or single mineral grains which did not fragment or volatilize during impact. By contrast, bulbous (type B) tracks, having large bulbous cavities and multiple terminal tracks, were likely produced by loosely bound fine-grained and/or volatile-rich impactors (Hörz et al. 2006). Particles are widely dispersed along the tracks (Flynn et al. 2006), and transmission electron microscopic (TEM) investigations are often required to distinguish cometary samples from surrounding compressed and/or melted aerogel. This makes organic studies of these samples an especially difficult endeavor, because the physical and chemical effects incurred by impact shock need to be deconvolved from the significant but variable contribution of contaminants from the aerogel itself (Sandford et al. 2006).

To address these challenges, we have developed new sample preparation and analysis techniques and applied these to the comprehensive documentation, survey, and analysis of entire aerogel tracks of Wild 2 samples. This

coordinated approach facilitates interpreting the properties of individual samples in the context of their spatial location in the parent track and the relationships to other particles within the same track. All sample documentation, processing, and analysis, from start to finish, were undertaken within the same facility, resulting in a detailed sample catalog.

For this study, our goals were to answer the following questions: (1) Are the fine grains along the track associated with the terminal particle, either mineralogically, chemically, or isotopically? (2) What are the proportions of melted and unmelted particles within a given track? (3) Do particle types differ systematically along the track, from the entrance hole all the way to the terminal particle? (4) Do carrot-type tracks contain organic matter? (5) Do the particle compositions characteristic of type A and B tracks differ in degree or kind?

Here, we present results of our analysis of the “carrot” type A aerogel track #112, hereafter T112 (Fig. 1) and the “bulbous” type B aerogel track #113, hereafter T113 (Fig. 2) from the nanometer to the millimeter scale. Scanning TEM (STEM) was used for elemental and detailed mineralogy characterization, NanoSIMS was used for isotopic analyses, and ultrafast two-step laser mass spectrometry (*ultra-L²MS*) was used to investigate the nature and distribution of organic phases. The isotopic measurements were performed on samples characterized in detail by TEM for coordinated mineralogy. This approach also enabled spatially resolving the target sample from fine-scale mixtures of compressed aerogel and melt.

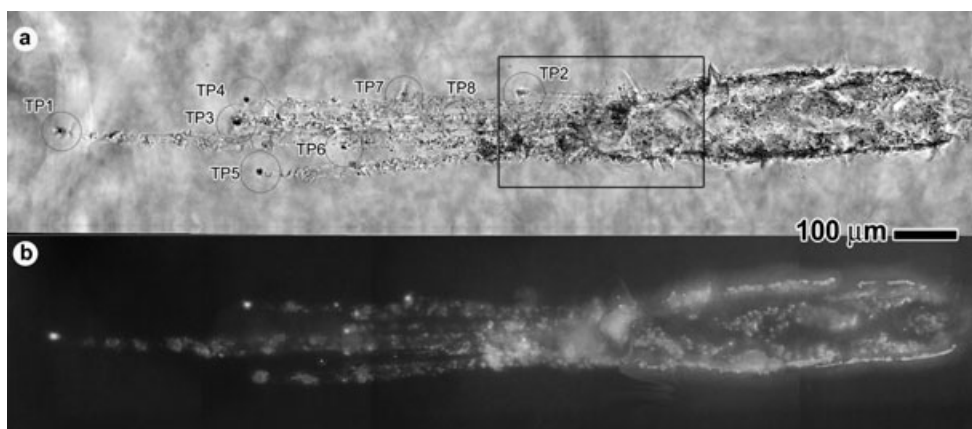
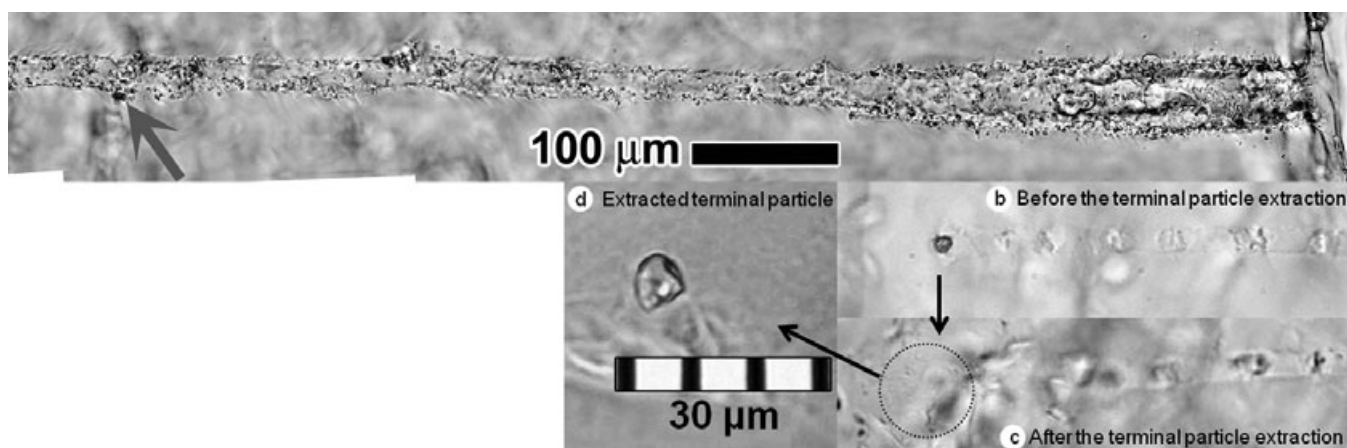


Fig. 2. T113 1466 μm long bulbous type track. a) Extended depth of field optical micrograph of T113. The ellipsoid bulb has an equatorial diameter of approximately 140 μm and extends into the aerogel from the initial impact point to a depth of approximately 600 μm . The thin terminal particle tracks radiating from the bulb base extend from a further approximately 400–800 μm . All of the eight extracted terminal particles are circled and named as TP1–TP8. The 150 \times 200 μm track wall area indicated by a box was removed from the keystone for further investigation by the STEM. By this track wall removal, lower portion of the track was exposed and used for $\mu\text{L}^2\text{MS}$ organic analysis. b) T113 under UV light in the same scale as (a).

SAMPLES, SAMPLE PREPARATION, AND ANALYTICAL METHODS

Sample

Prior to any sample processing, we first undertook a comprehensive photodocumentation of the sample using extended depth-of-field microscope imaging. In this technique, the sample is imaged as a series of through focus micrographs to produce an image stack such that any point within the sample is in focus within one or more of the frames within the image stack. By applying a

complex-wavelet-based algorithm (Forster et al. 2004), a single image can be produced for which the depth-of-field spans the entire focus range of the sample. In addition to optical imaging, we also used UV illumination at approximately 380 nm to capture the sample fluorescence image which proved helpful in discriminating compressed aerogel from indigenous cometary material.

Track #112

This 1947 μm long type A (carrot) track was extracted from aerogel tile C2067 as a keystone (Fig. 1a) and has one distinct terminal particle ($\sim 6 \mu\text{m}$ in

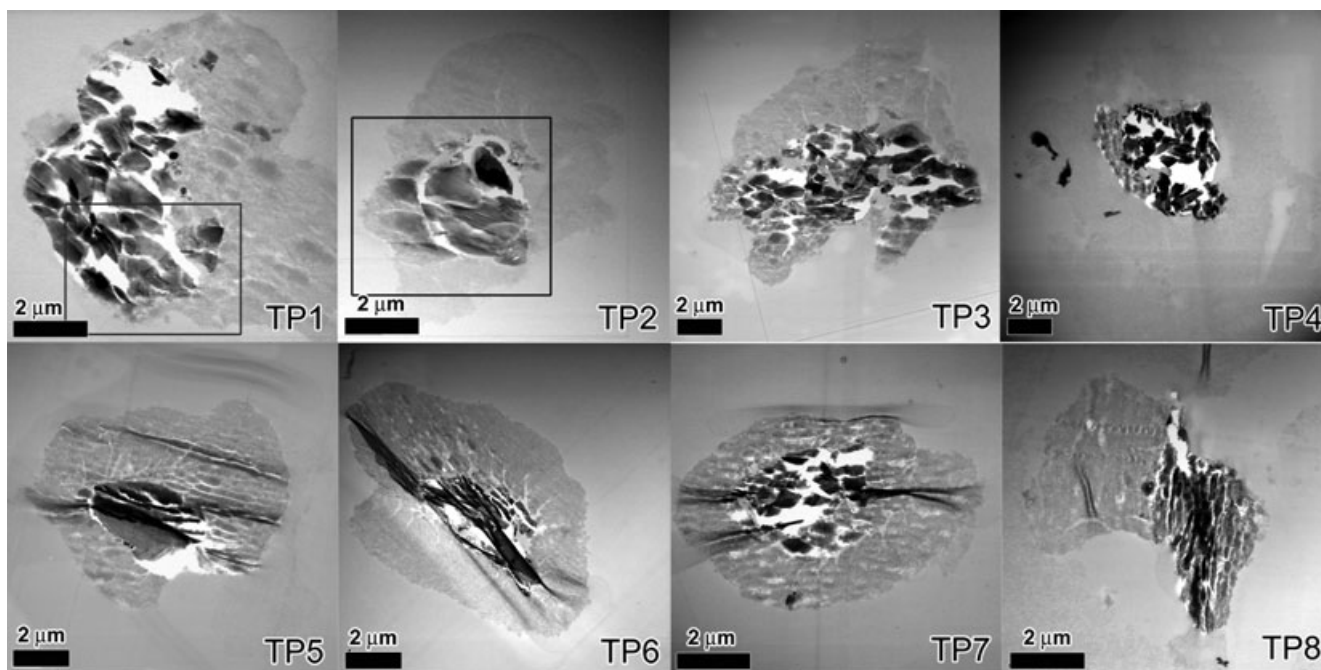


Fig. 3. Bright-field STEM micrographs of ultramicrotome thin sections of eight terminal particles from T113. The sample name TP# is corresponding to the numbers in Fig. 2a. All terminal particles except TP1 and TP8 have a core-mantle structure of compressed-molten aerogel (mantle) and cometary material in the center.

diameter; Fig. 1b). See Westphal et al. (2004) for more details on the aerogel keystone extraction technique.

Track #113

This 1466 μm long bulbous track was extracted from aerogel tile C2061 as a keystone. T113 has a type B morphology (Hörz et al. 2006). The track is characterized by a bulbous ellipsoidal cavity extending down from the point of impact to a base from which approximately a dozen long slender terminal particle tracks radiate. T113 was photo documented with the same manner as T112 (Fig. 2). Eight distinct terminal particles (4–8 μm in diameter; Figs. 2 and 3) were extracted from T113.

Terminal Particle Extraction and Sectioning

After the depth-of-field photodocumentation, all the terminal particles of T112 and T113 were removed and processed separately. The terminal particles were gradually exposed by carefully removing the surrounding aerogel with a glass needle, and the end result of this operation (before and after the particle extraction) is shown in Figs. 1b and 1c. The T112 terminal particle was removed from the keystone with minimal damage to the rest of the track. The removed terminal particles were then temporarily stored between two dimpled glass slides for further photodocumentation (Fig. 1b). The terminal

particles were then embedded in low-viscosity epoxy (EMbed812), and left to cure in a vacuum oven at 70 °C for 48 h. After curing, the samples were sliced into 70 nm thick thin-sections using a Leica EM UC6 ultramicrotome, equipped with a 35° diamond knife. The sections were floated onto ultrapure water and transferred to six amorphous C film-supported Cu TEM grids for the TEM and NanoSIMS studies. The epoxy potted butts with remaining part of the terminal particle were used for the $\mu\text{L}^2\text{MS}$ study.

Dissection of Tracks in Aerogel

After the terminal particle removal, we embedded T112 in epoxy and sectioned the entire block by ultramicrotomy. Previous workers have embedded and microtomed entire Stardust tracks, by first compressing the tracks followed by embedding and sectioning (Matrajt and Brownlee 2006). That approach offers the advantage of spatially concentrating the captured particles, and thereby improving the efficiency of TEM and mineralogical surveys. Here, we used a different method, specifically avoiding any track compression before embedding the track in resin, so that our microtome sections preserved the original shape and size of the track. We began by gently placing the keystone containing T112 on a very thin layer of EMbed812 epoxy and heated it at approximately 70 °C under vacuum for

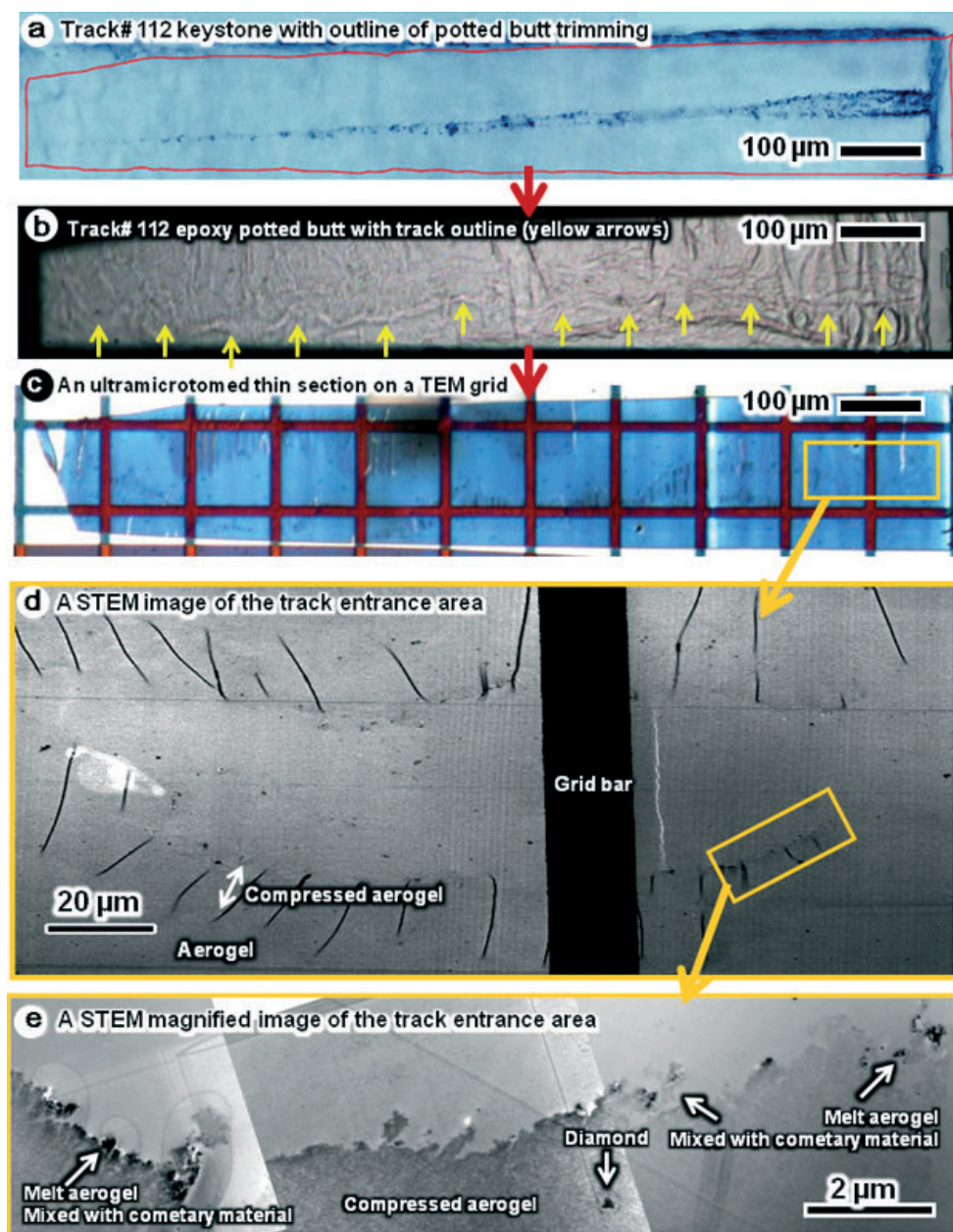


Fig. 4. Processing flowchart of dissect the whole track in aerogel. a) Low-magnification optical micrograph (under transmitted light) of the T112 keystone after the terminal particle extraction. The red trapezoid indicates the outline of trimmed potted butt. b) Top view of the epoxy potted butt of T112 after trimming into trapezoid shape. Yellow arrows indicate the track outline visible through the covering epoxy resin. c) One of 510 ultramicrotomed thin sections of T112 mounted on amorphous carbon supported Cu TEM grid. d) A bright-field STEM micrograph of the boxed area in Fig. 3c. The track morphology is well-preserved in an ultramicrotome thin section and material is intact. The aerogel within 20 μm of the track wall (darker contrast with wrinkles) was compressed by the impact. e) Photomosaic of bright-field STEM micrographs of boxed area in Fig. 3d. Numerous submicrometer-sized grains are observed along the track wall. Many of these tiny grains consist of melt particles (cometary material intimately mixed with melted aerogel). One of the diamond grains (Fig. 8a) is located in the compressed aerogel (arrowed).

a couple of hours. Additional aliquots of epoxy were added little by little under vacuum until the keystone was completely impregnated by epoxy. After curing for 48 h, the epoxy block was then trimmed along the length of the track (Figs. 4a and 4b). A total of 510 thin sections

(70 nm thickness) were created track-lengthwise using a Leica EM UC6 ultramicrotome and mounted on 105 different amorphous C film-supported Cu TEM grids (Fig. 4c). Eighty-six thin sections were thoroughly examined by STEM.

For T113, a $150 \times 200 \mu\text{m}$ area including the upper track surface and attached aerogel was removed from the T113 keystone (boxed area of Fig. 2) and processed in the same manner as T112 dissection. The exposed area of the main T113 keystone was later analyzed by *ultra-L²MS* for its distribution of organic compounds.

Analytical Methods

Transmission Electron Microscope

Imaging and selected area electron diffraction (SAED) were performed using a JEOL 2000FX TEM (200 keV) and a JEOL 2500SE field-emission STEM. The STEM is equipped with a large area, thin window energy-dispersive X-ray detector (EDX) analysis system, and Gatan electron energy-loss spectra imaging filter. Nanometer-scale compositional maps of samples were acquired with a 2 or 4 nm incident probe diameter. Image layers of each mapped region were acquired and combined to achieve sufficient counting statistics to derive quantitative abundances for major elements (e.g., O, Mg, Al, Si, S, Ca, Fe, and Ni) in each pixel. Typical acquisition times for the 256×200 pixel spectrum images were 30–45 min which gave detection limits of approximately 0.1 atom% for most elements. The EDX data were reduced using the Cliff–Lorimer method (Cliff and Lorimer 1975).

Interplanar spacings were measured from the SAED patterns and calibrated against an Au standard. The measured *d*-value error is $\pm 0.04 \text{ \AA}$. The values of camera length were calibrated at the same accelerating voltage and objective lens setting using an evaporated Au standard.

NANOSIMS

The isotopic imaging studies were performed with the Johnson Space Center Cameca NanoSIMS 50L ion microprobe. All isotopic measurements were performed after the TEM analysis. The O isotopic images were acquired by rastering a 1–2 pA 16 keV Cs primary ion beam over areas of approximately $10 \times 10 \mu\text{m}$, while simultaneously acquiring ^{16}O , ^{17}O , $^{18}\text{O}^-$, $^{28}\text{Si}^-$, and $^{24}\text{Mg}^{16}\text{O}^-$ secondary ion counts with five electron multipliers. Multiple (10–25) image scans were acquired for each sample. Image acquisition times ranged from 3 to 10 h, consuming 30–100 nm of surface material. High-mass resolution scans showed that the contribution of $^{16}\text{OH}^-$ to the $^{17}\text{O}^-$ peak was $< 1\text{‰}$, with a mass-resolving power of at least 9000 (Cameca definition), or approximately 6000 in the conventional definition. The mass peaks were centered in the exit slits of each detector prior to the image runs and the ^{16}O peak was re-centered

every 30 min. Motion of the ^{16}O peak was very small, and shifts were applied to all other peaks. The magnetic field was controlled with a nuclear magnetic resonance probe, which kept peak positions stable to $\Delta M/M < 5$ ppm. Thin sections were coated with 50 \AA of Au, and an electron flood gun was used to compensate sample charging. Isotopic compositions of target samples were determined with isotopic image processing software developed at JSC. The perimeters of the target minerals were determined in the ion images by reference to TEM images of the samples and by $^{24}\text{Mg}^{16}\text{O}^-/^{16}\text{O}^-$ ratio images, which clearly distinguish crystalline silicates from Mg-free aerogel.

For the C and N isotopic measurement, we obtained images of $^{12}\text{C}^-$, $^{13}\text{C}^-$, $^{16}\text{O}^-$, $^{12}\text{C}^{14}\text{N}^-$, $^{12}\text{C}^{15}\text{N}^-$, and $^{28}\text{Si}^-$ in multidetection. The isotopic images were obtained from an $8 \times 8 \mu\text{m}$ field of view. We acquired 30 sequential images over a period of 6 h with a 0.5 pA primary ion current. A nearby ($< 100 \mu\text{m}$) terrestrial grain of 1-hydroxybenzotriazole hydrate was measured as N isotopic standards and USGS24 graphite as C isotopic standards prior to measuring the sample. The TEM carbon film substrate served as a secondary isotopic standard, helping to ensure that the tuning conditions did not change substantially during the measurement.

The O, C, and N isotopic compositions are reported as delta values, representing the deviation of the measured isotopic ratios with terrestrial standards in parts per thousand (‰):

$$\delta R = \frac{R_{\text{measured}}}{[R_{\text{standard}} - 1] \times 1000} \quad (1)$$

The C isotopic reference is Pee Dee Belemnite, the N isotopic reference is air, and the O isotopic reference is standard mean ocean water (SMOW).

$\mu\text{L}^2\text{MS}$

No specific sample preparation treatments are required for *ultra-L²MS* analysis other than the surface to be analyzed be physically unobstructed. For the in situ analysis of track walls, this simply requires the dissection and manual removal of the upper track hemisphere and overlying aerogel so as to expose the lower interior track surface. To secure physically the section to a sample platter for introduction into *ultra-L²MS* instrument, we devised an organic-free friction mounting scheme whereby the aerogel sample is sandwiched under a slight compressive load between two 95% transmission stainless steel electroformed meshes. In the case of terminal particles, analysis is complicated by the presence of exterior rind of compacted and/or melted aerogel, which can fully encapsulates the particle. Direct analysis

of such particles would hence only reveal information on this exterior silica shell and not on the underlying particle. Consequently, this necessitated particle extraction followed by mounting in epoxy and partially sectioning using an ultramicrotome so as to expose the interior cross sectional surface. This approach is also complementary to sample preparation requirements of TEM and NanoSIMS, with the cut thin-sections being used for the mineralogical and/or isotopic characterization. Although the mounting epoxy substrate is organic, it does not significantly contribute to the organic species observed by *ultra-L²MS* instrument since epoxy, being a macromolecular polymer, cannot be desorbed under neutral conditions. For the technical and analytical details of *ultra-L²MS* instrument, see Clemett et al. (2010).

RESULTS

T112 Terminal Particle: Mineralogy, Chemistry, and Oxygen Isotopes

The terminal particle of track T112 is a rounded, approximately 6 μm in diameter, single crystal of forsterite with minor chromite, surrounded by compressed aerogel and melted material (Fig. 5a). Nanometer-scale X-ray spectral mapping reveals that the core of the forsterite grain is Fo_{99} and shows a slight enhancement in Fe in the outermost approximately 10–20 nm of the grain to Fo_{97} (Fig. 5b). High-resolution imaging and SAEDs show that the forsterite grain is strained and contains a high density ($\sim 2 \times 10^{10} \text{ cm}^{-2}$) of parallel planar defects oriented along (100) (Fig. 5c).

O isotopic images of the forsteritic terminal particle show a homogeneous O isotopic composition which is significantly ^{16}O -rich: $\delta^{17}\text{O} = -48.7 \pm 4.5\text{‰}$, $\delta^{18}\text{O} = -41.4 \pm 3.1\text{‰}$ (1σ) (Fig. 6). The forsterite grain is partially bordered by a thin rind of forsteritic olivine mixed with melted aerogel, and this material shows an intermediate ^{16}O enriched composition of $\delta^{17}\text{O} = -23.2 \pm 9\text{‰}$ and $\delta^{18}\text{O} = -24.0 \pm 6\text{‰}$, indicating approximately 50% of the O derives from melted aerogel, assuming the embedded olivine is similarly ^{16}O -enriched as the main mass of the terminal particle. This is consistent with chemical measurements of the rim material. No O isotopic difference is evident between the forsterite core (Fo_{99}) and the slightly Fe-enriched rim (Fo_{97}).

T112 Organic Analysis

The terminal particle after extraction and epoxy sectioning was analyzed by *ultra-L²MS*. No evidence was found for the presence of any organic component.

T112 Track Mineralogy

The track morphology is well-preserved in ultramicrotome thin sections and material is intact. The aerogel within 20 μm of the track wall (darker contrast in Fig. 4d) was compressed by the impact event. Numerous submicrometer-sized grains are observed along the track wall. Many of these tiny grains consist of only molten aerogel, containing no detectable Mg which could be an indicator of trace of cometary material. Many other tiny grains consist of melt particles in which cometary material is intimately mixed with melted aerogel (Figs. 4e and 7a–c). EDX spectra obtained from the mixed particles show strong enrichments in Si, and minor Mg, Ca, S, Cr, and Fe.

There are tens of dark contrast relatively bigger grains (10–30 μm in size) along the aerogel track (Fig. 1a). These grains consist of compressed aerogel segregated from the track wall and surrounded by the above-described melted aerogel (Fig. 7d). We identified one crystalline enstatite grain (200 nm in size) encapsulated in melt aerogel but no forsterite grains were found.

We also identified six diamond grains (100–350 nm in size) both along the track and inside the compressed aerogel area (Fig. 8). These diamond grains were encapsulated by molten aerogel and an outer rind of compressed aerogel and were located at the edge of the track together with other cometary grains. We determined the C isotopic compositions of one of the diamond grains to be $\delta^{13}\text{C} = -10.9 \pm 9\text{‰}$ (1σ). The N isotopic composition of the diamond was also normal within large errors owing to very low N concentration ($\delta^{15}\text{N} = 47 \pm 142\text{‰}$, 1σ).

T113 Terminal Particles: Mineralogy, Chemistry, and Oxygen Isotopes

Eight terminal particles were extracted and analyzed from T113 (Fig. 3). The mineralogy of these particles is dominated by coarse-grained enstatite (En_{90}) that is largely orthoenstatite with minor, isolated clinoenstatite lamellae (Fig. 9). One terminal particle (TP1) contains minor forsterite (Fo_{88} ; Fig. 10) and small inclusions of diopside with % levels of Al, Cr, and Fe. The diopside has Cr/Fe atomic ratio of approximately 3 (Fig. 10). Two of the terminal particles (TP1 and TP3; Fig. 6) contain angular regions of fine-grained nepheline surrounded by enstatite (Fig. 11). Diffraction analysis and dark-field imaging showed that the nepheline is polycrystalline and EDX analyses found no detectable K (Fig. 11). Some of the nepheline grains are partly vesiculated.

We measured the O isotopic compositions of two enstatite grains (TP2 and TP3) from T113, and found

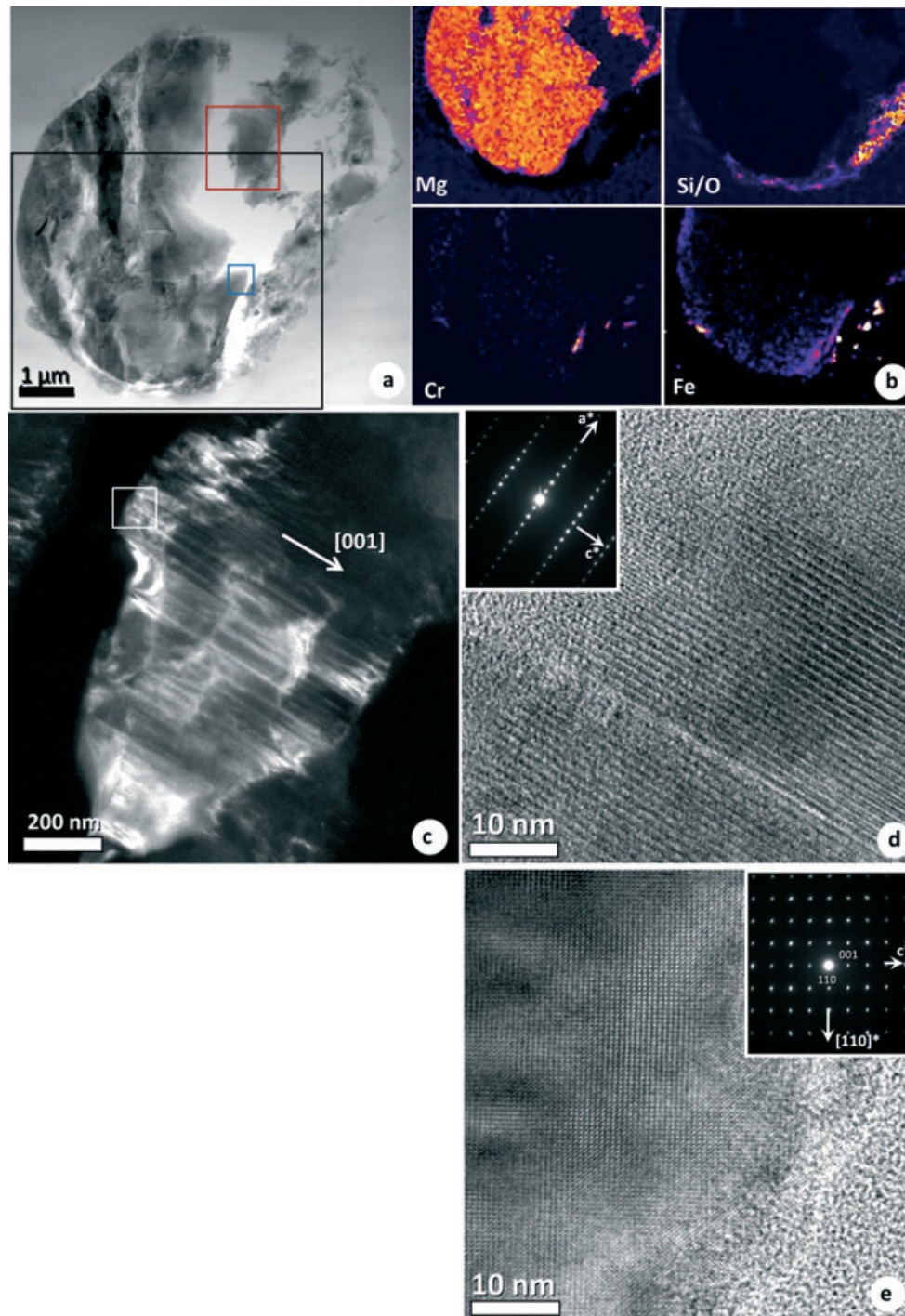


Fig. 5. Mineralogy and chemistry of the terminal particle of T112. a) A bright-field STEM micrograph of an ultramicrotomed thin section of T112 terminal particle. b) Nanoscale elemental X-ray (Mg, Si/O, Cr, Fe *K*-lines) maps of the black boxed area in (a). These X-ray maps reveal that the terminal particle is forsterite 99 with minor chromite, minor compressed aerogel, and melted material. The Fe map shows a slight enhancement in Fe toward the rim of the grain to Fo₉₇. c) A dark-field TEM micrograph of a forsterite grain in the red boxed area of (a). A high density of (100) planar dislocations. The corresponding SAED pattern is shown as (d) inset. d) A high-resolution TEM micrograph of the boxed area and taken along the same direction as (c), [010] direction. The forsterite is highly strained with numerous (100) planar defects. e) A high-resolution TEM micrograph of the blue boxed area in (a). Inset shows the corresponding SAED pattern.

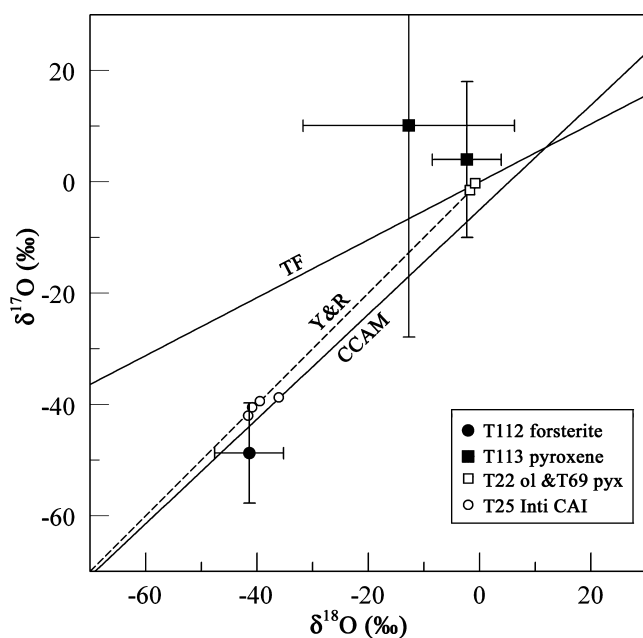


Fig. 6. Oxygen isotopic compositions of T112 forsterite (solid circles) and T113 pyroxene (solid squares) compared with the Stardust CAI particle Inti (T25, open circles) and large olivine (T22) and pyroxene (T69) grains (open squares). The T25, T22, and T69 data are taken from McKeegan et al. 2006. The terrestrial fractionation line (TF), the CAI or carbonaceous chondrite anhydrous mineral (CCAM) trend line, and the Young and Russell (Y&R) slope 1 line are shown for comparison.

them to be terrestrial within error: TP2: $\delta^{17}\text{O} = 10 \pm 19\text{‰}$, $\delta^{18}\text{O} = -12.7 \pm 9.5\text{‰}$; TP3: $\delta^{17}\text{O} = 4.0 \pm 7.0\text{‰}$, $\delta^{18}\text{O} = -2.3 \pm 3.1\text{‰}$ (1σ).

T113 Organic Analysis

Terminal track particles and an interior section of the main track cavity were investigated by *ultra-L²MS*. Of the eight discrete terminal particles extracted from the aerogel keystone, two particles (TP1 and TP3) unambiguously showed the presence of organic matter. A weak but diffuse distribution of organic species was also identified coating the interior surface of an approximately 300 μm long section of the main track cavity located toward the bulb base. Integrated mass spectra are shown for these four samples in Fig. 12. In all cases, spectra were acquired under identical experimental conditions. Comparison of relative peak heights between the spectra of the different terminal particles is meaningful, although caution needs to be exercised when comparing to the spectrum obtained from aerogel track surface due to the higher surface area sampled. The presence of a mass peak at 106 amu assignable to a 2-methylbenzene isomer has an uncertain origin since 1,4-dimethyl benzene ($\text{CH}_3\text{-C}_6\text{H}_4\text{-CH}_3$;

106.078 amu) is used in *ultra-L²MS* instrument as an internal mass calibrant.

Terminal Particles

The organic signatures of TP1 and TP3 are of particular interest. While both demonstrated significant spectra complexity, indicating a wide diversity of organics, the two distributions are clearly dissimilar although mineralogically both particles are essentially enstatite grains. TP1 showed the highest abundance of organics characterized by a distribution of 1–3 fused-ring aromatic hydrocarbons and their associated alkylated homologs ($\text{Ar-(CH}_2)_n\text{-H}$; $n = 1, 2, 3 \dots$). The principal peaks at 94, 128, and 178 amu correspond to phenol ($\text{C}_6\text{H}_5\text{-OH}$), naphthalene (C_{10}H_8), and phenanthrene ($\text{C}_{14}\text{H}_{10}$), respectively. While the spectral complexity is greater than what we observed from C1 or C2 carbonaceous chondrites under the same experimental conditions (Clemett et al. 2010), the dominant peaks and associated alkylation series are nevertheless broadly similar. We interpret the outlying peak at 254 amu to represent dimerized naphthalene that can readily be formed via thermally induced free radical polymerization ($2\text{Ar-H} \rightarrow 2\text{Ar}^\bullet + 2\text{H}^\bullet \rightarrow \text{Ar}_2 + \text{H}_2$) and hence may have formed during aerogel capture. By contrast, the mass spectrum of TP3 is dominated by several primary peaks that do not show prominent homologous alkylation series. The peaks at 94, 166, and 178 amu corresponding to phenol ($\text{C}_6\text{H}_5\text{-OH}$), fluorene ($\text{C}_{13}\text{H}_{10}$), and phenanthrene ($\text{C}_{14}\text{H}_{10}$), respectively. The peaks at 91 and 213 amu are however not easily assigned based on comparison with carbonaceous chondrite spectra (Clemett et al. 2010).

Track Bulb

While the concentration of organic matter associated with the interior surface of the main track cavity is low relative to the three carbonaceous terminal particles, it is distributed over a substantially greater surface area. Consequently, the bulk of the organic matter associated with the original impacting particle resides in the main track cavity rather than the individual terminal particles. The mass envelope of the observed organics demonstrates a pronounced expansion to higher mass species compared to the terminal particle spectra. In addition to the fused ring aromatic species identified in the terminal particle spectra, a number of prominent odd mass species are evident at 167, 219, 223, and 267 amu that we interpret to represent aromatic nitriles species (Ar-CN) similar to those previously reported from Stardust aerogel tracks (Clemett et al. 2010). In addition, several alkylation series (e.g., 282, 296, 310, and 324 amu) are evident in the high mass region although the dominant peaks at 294 and 338 amu do not correspond

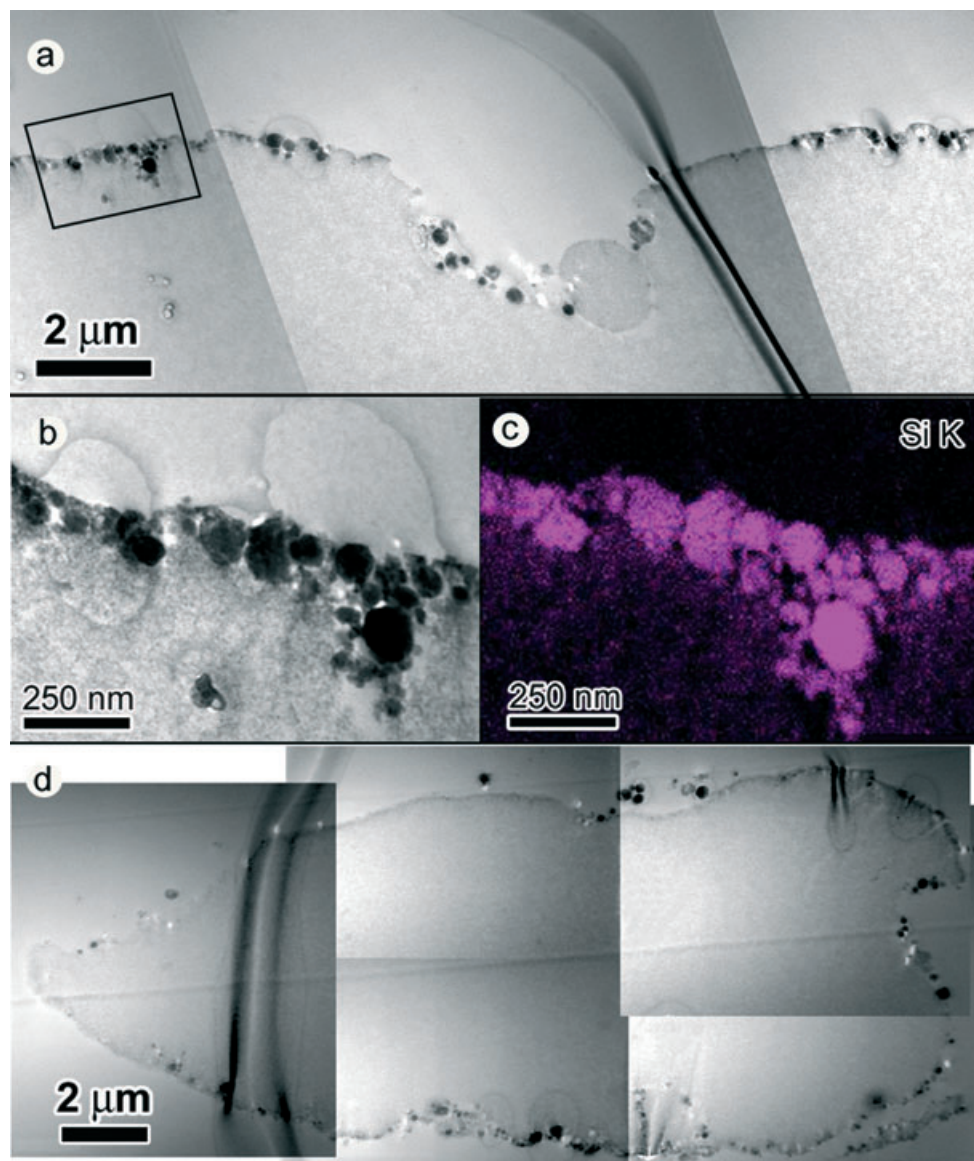


Fig. 7. Main texture along the aerogel track wall of T112. a) A photomosaic of low-magnification bright-field STEM micrographs of a part of the track wall. The aerogel edge is filled with molten aerogel beads. A spherical object in the middle is compressed aerogel. b) A bright-field STEM micrograph of the boxed area in (a). c) A nanoscale elemental Si *K*-line X-ray map of the same area as (b). d) A photomosaic of low-magnification bright-field STEM micrographs of a dark contrast object along the track wall (red arrow in Fig. 1a). This object seemed to be a cometary fragment in the optical micrograph of Fig. 1a; however, it turned out that this is a compressed aerogel surrounded by molten aerogel the same as the track wall.

to any of the simple aromatic hydrocarbons commonly observed in carbonaceous or ordinary chondrites.

DISCUSSION

Terminal Particle Versus Materials Along the Carrot Track

We have demonstrated the ability to ultramicrotome an entire track along its axis without first compressing

the aerogel. This innovation allows us to examine the distribution of fragments along the entire track from the entrance hole all the way to the terminal particle. This sample preparation technique preserves the sample well, with no evidence for significant loss of sample during microtomy.

For T112, we observed that the mineralogy of fragments along the track axis was different from that of the terminal particle. The fragments are dominated by melt particles that result from the interaction of the

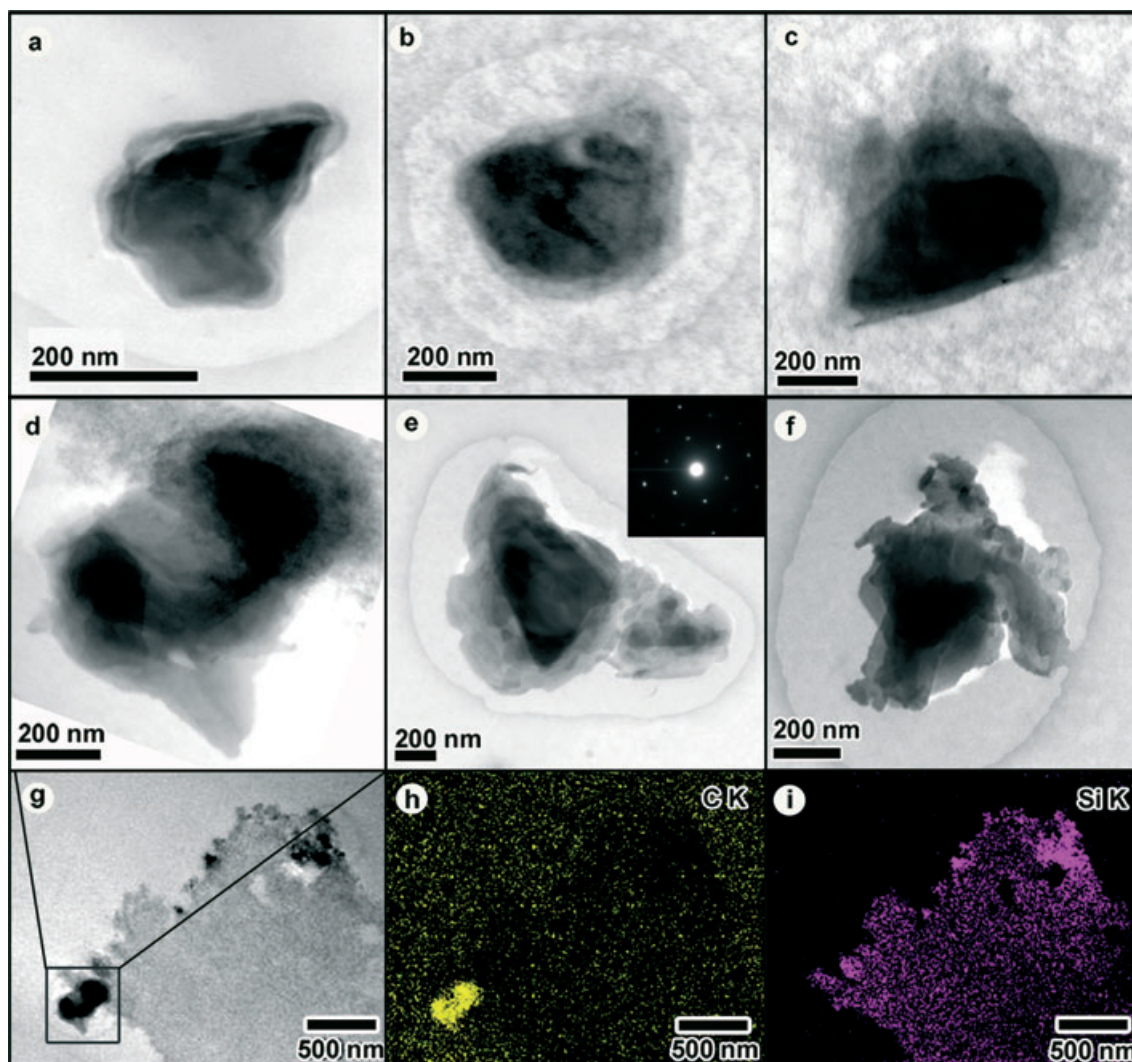


Fig. 8. Diamond grains found along the aerogel track wall of T112. a–f) Bright-field STEM micrographs of six diamond grains observed in compressed aerogel. Inset shows an SAED pattern from the diamond grain of (e). g) A low-magnification bright-field STEM micrograph of track wall with compressed and melted aerogel and an embedded diamond grain shown in (d). h) A nanoscale elemental C *K*-line X-ray map of the area of (g). i) A nanoscale elemental Si *K*-line X-ray map of the same area as (g).

impacting particle with molten aerogel. Surveying 16% of the entire aerogel track wall (81 of 510 thin sections were thoroughly observed), we found only one crystalline enstatite grain (200 nm in size) encapsulated in melt aerogel. We estimate that the terminal particle contains 90% of the mass of the impactor (mass of total fine particles along the track: mass of 6 μm terminal particle = 1:10).

Origin of the Terminal Silicate Particles

The combined mineralogical and O isotopic measurements of crystalline silicates have implications for the origins of cometary materials. The identification of crystalline silicates in comets by infrared spectroscopic

observations (Hanner et al. 1994; Crovisier et al. 1997) challenged the conventional wisdom that comets were minimally altered remnants of interstellar materials, which are dominated by amorphous silicates. Infrared spectroscopic surveys of dust in the galaxy have placed an upper limit on the crystalline mass fraction of interstellar silicates of approximately 2% (Kemper et al. 2004). Crystalline silicates in comets have thus been proposed to be products of high-temperature process in the solar system, either forming by direct condensation from high-temperature gas or annealing of amorphous interstellar grains (Hanner et al. 1994). Many of the olivine and pyroxene grains in comet Wild 2, including those studied here, are likely vapor phase condensates. It is unlikely that the crystalline silicates formed by

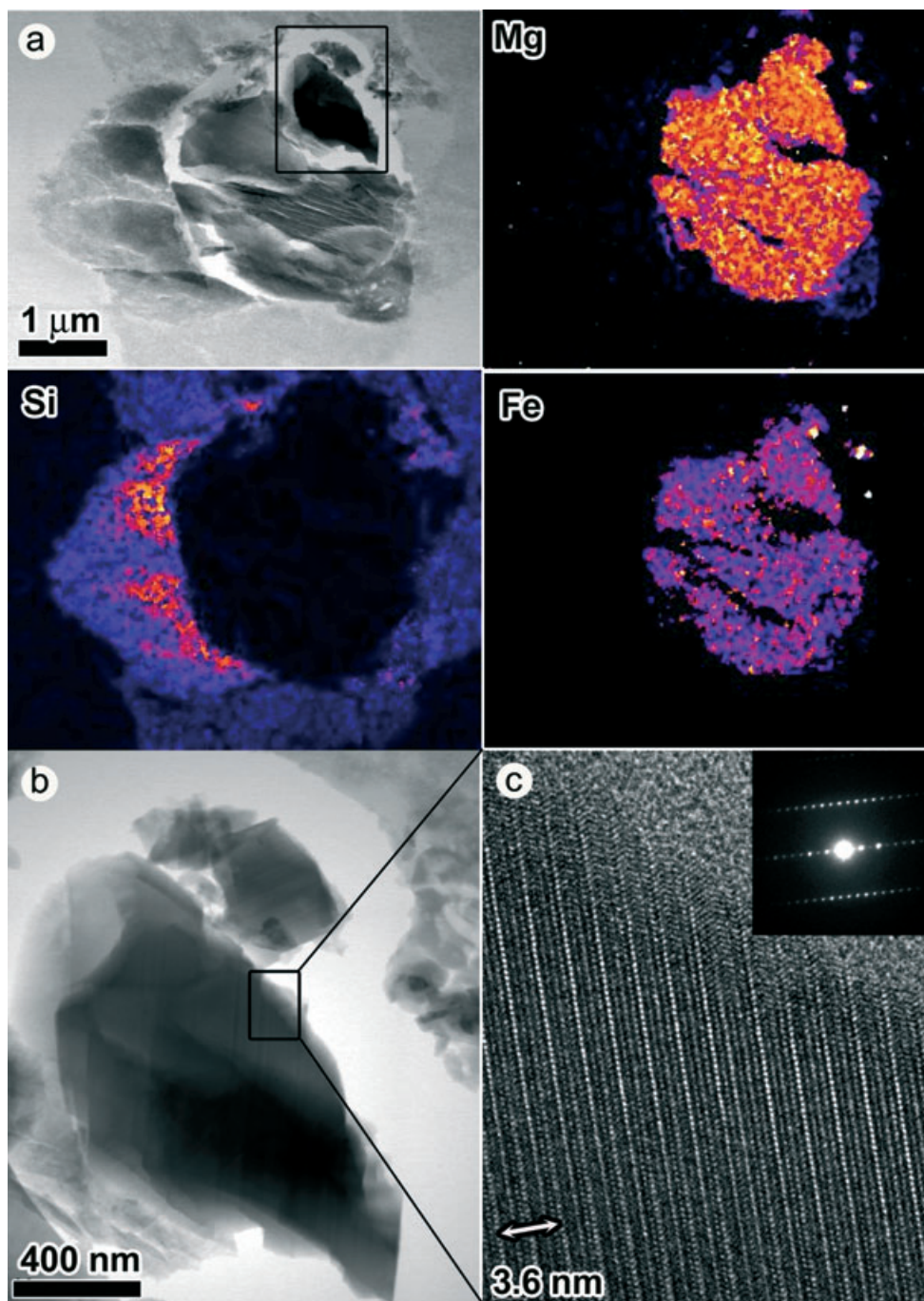


Fig. 9. Mineralogy, chemical composition, and crystallography of the terminal particle TP2 of T113. a) A bright-field STEM micrograph and nanoscale X-ray elemental maps of Mg, Si, and Fe *K*-lines of the boxed area in Fig. 3 on TP2. b) A bright-field TEM micrograph of an enstatite single grain of the boxed area in (a). c) A high-resolution TEM micrograph of the boxed area of (b). The 18 Å fringe spacing is associated with orthoenstatite, whereas the 9 Å fringe spacing corresponds to clinoenstatite. In this figure, the clinoenstatite appears as isolated double (100) lamellae within the orthoenstatite matrix. Inset shows an SAED pattern corresponding to the same area.

annealing of amorphous precursors because such grains tend to have nonstoichiometric compositions and the annealed products are polycrystalline. Certain other polymineralic objects observed with amorphous silicate

matrices are, however, consistent with annealing of amorphous precursors (Zolensky et al. 2006).

The O isotopic compositions of most Wild 2 samples are within the range of meteoritic materials,

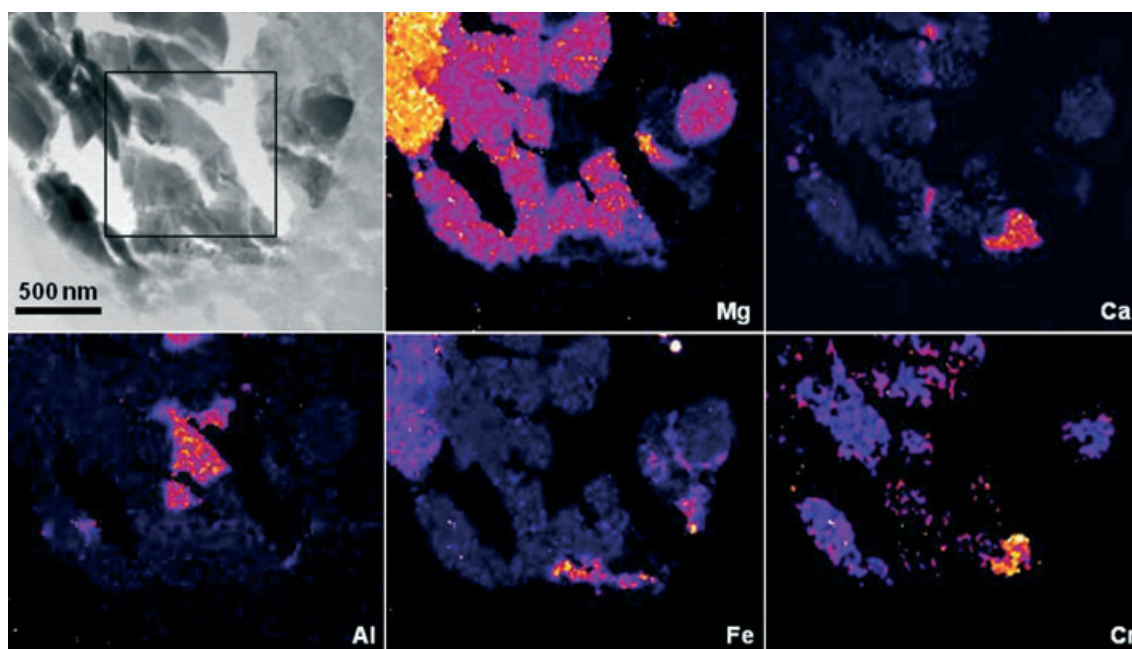


Fig. 10. Chemical compositions of TP1 of T113: A bright-field STEM micrograph of the boxed area of TP1 of T113 in Fig. 3 and its nanoscale X-ray elemental maps of Mg, Ca, Al, Fe, and Cr *K*-lines of the same area.

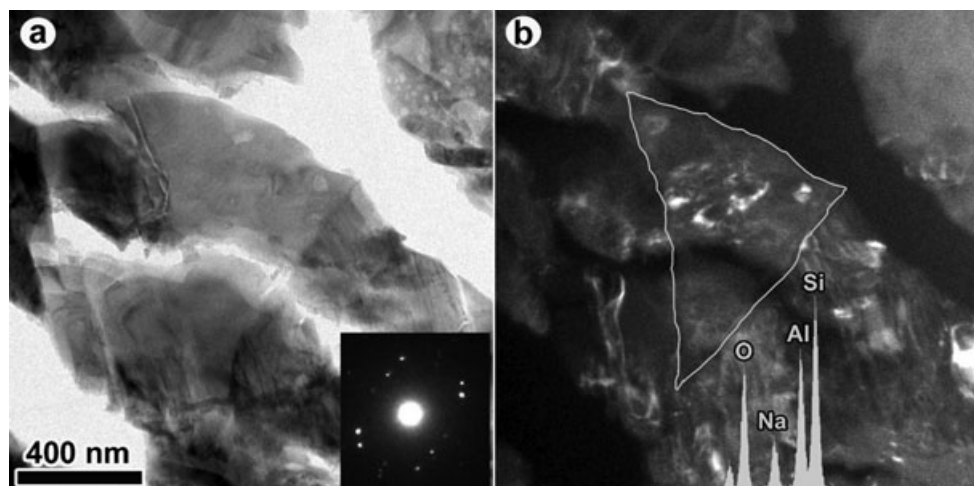


Fig. 11. Texture, mineralogy, and chemistry of nepheline in TP1 of T113. a) A bright-field STEM micrograph of the boxed area of Fig. 10. The nepheline is embedded in enstatite matrix. Inset shows corresponding SAED pattern from the nepheline. b) A dark-field STEM micrograph of the same area of (a). Yellow outline shows the boundary of nepheline phase. Inset shows the corresponding EDX spectra from the nepheline phase.

with the majority having near terrestrial values (McKeegan et al. 2006). The T113 terminal particles we measured had terrestrial O isotopic compositions within error (Fig. 6). The precision of these measurements is limited by the small sample size coupled with the state of the sample (microtome thin section surrounded by aerogel). Nevertheless, the isotopic compositions of

these grains distinguish them from typical values of presolar silicates. Furthermore, these two particles are simple mineral grains and are more likely to have formed by condensation rather than annealing. These isotopic and mineralogical properties are most consistent with the silicate grains having formed within the solar nebula.

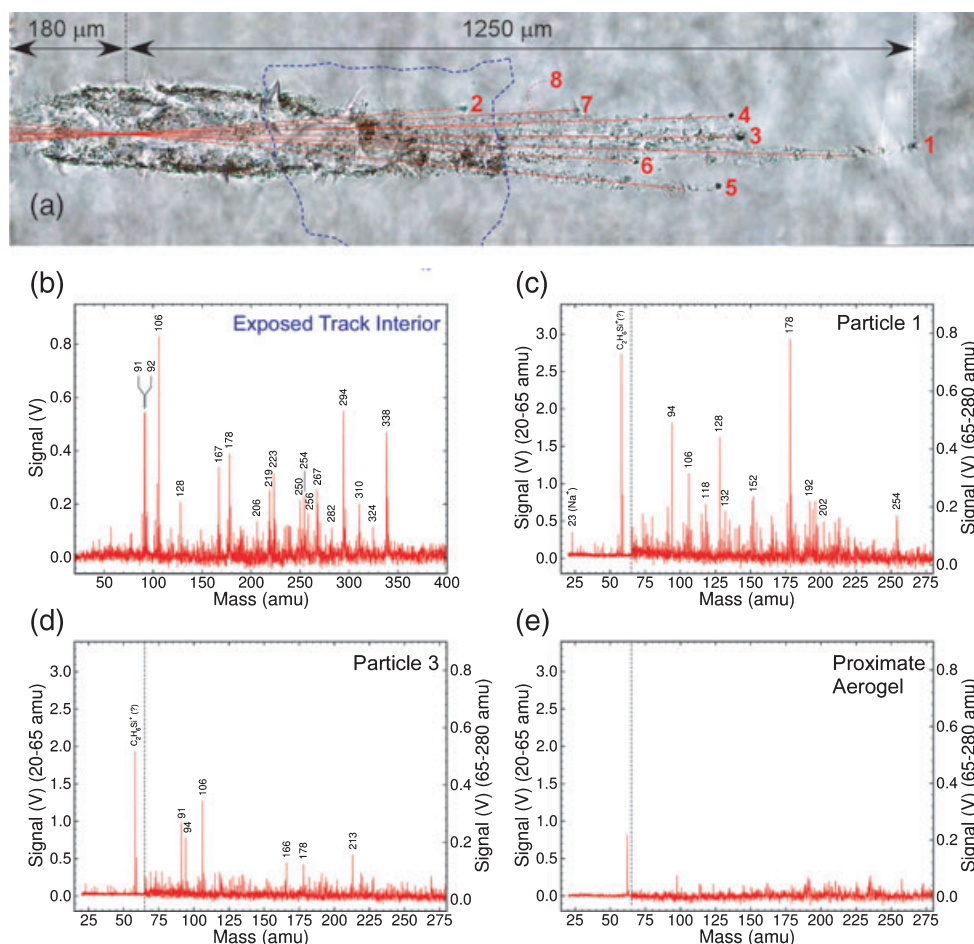


Fig. 12. a) Extended depth-of-field optical image of track T113 in aerogel keystone prior to analysis. The nine principal terminal particles are shown by their respective numbers labeled in red, along with their estimated trajectory vectors shown by the red lines that intersect approximately 180 μm below the aerogel impact surface. The region enclosed by the blue dashed line represents the section of the aerogel track that was exposed for the analysis of the interior track cavity. b–d) *ultra-L²MS* of the interior track main cavity and the two terminal particles TP1 and TP3 that demonstrated an organic signatures. All spectra were acquired under identical experimental conditions and prominent peaks are labeled with their mass in amu. Mass peak at 106 amu coincides with that of 1,4-dimethyl benzene used as an internal mass calibrant and should be ignored. e) *ultra-L²MS* of the proximate aerogel area.

One of the most important findings of the Stardust mission has been the discovery of large, refractory grains having isotopic and mineral affinities to calcium-aluminum-rich inclusions (CAIs) and chondrules. These samples include the CAI-like particle Inti ($\delta^{17}\text{O}, \delta^{18}\text{O}_{\text{SMOW}} \cong -40\%$) (McKeegan et al. 2006) and three fine-grained olivine/pyroxene chondrule-like terminal particles from the Wild 2 cometary aerogel track #108 whose O isotopic composition is heterogeneous and falls along the carbonaceous chondrite anhydrous mineral (CCAM) line with $\delta^{17}\text{O}$ and $\delta^{18}\text{O}$ values ranging from approximately 0 to -45% (Nakamura et al. 2008, 2009). The forsterite terminal particle of T112 has a ^{16}O -rich composition that is identical within error to that of the Inti “CAI,” falling

near the endpoint of the CCAM trend line (Fig. 6). The isotopic, mineralogical, and chemical compositions of T112 terminal particle are similar to components of (1) forsterite-rich olivine inclusions in the Murchison (CM2) and Yamato-86009 (CV3) carbonaceous chondrites ($\delta^{17}\text{O}, \delta^{18}\text{O}_{\text{SMOW}} \cong -50\%$; Hiyagon and Hashimoto 1999), (2) amoeboid olivine aggregates (AOAs; $\delta^{17}\text{O}, \delta^{18}\text{O}_{\text{SMOW}} \cong -50\%$; Krot et al. 2002), and (3) a unique chondrule ($\delta^{17}\text{O}, \delta^{18}\text{O}_{\text{SMOW}} \cong -75\%$) in the Acfer 214 CH carbonaceous chondrite (Kobayashi et al. 2003). Overall, the terminal particle of T112 is most similar to components within AOAs. Although T112 is far smaller than AOAs in meteorites, it is similar in size to the typical individual olivine constituents of AOAs (Fagan et al. 2004). The mineralogical and isotopic properties of

AOAs point to condensation from a high-temperature gas, perhaps in the CAI-forming region but at somewhat lower temperatures (~ 1300 K; Grossman and Steel 1976; Wood 2004). The slight Fe-enhancement in the rim of T112 is consistent with minor alteration after formation, possibly by reaction with nebular gas at approximately 800 K or as a result of reactions occurring the aerogel capture event (Grossman and Steel 1976).

Comet 81P/Wild 2 thus appears to have the same diversity of high-temperature inner solar system nebular components found in meteorites: CAIs (McKeegan et al. 2006), chondrules (Nakamura et al. 2008, 2009), and AOAs (this study). These ^{16}O -rich high-temperature components are accompanied by abundant crystalline silicates having near-terrestrial O isotopic compositions, further showing that comet Wild 2 also sampled a similarly wide range of O isotopic reservoirs to that observed in meteorites. The abundant isotopically solar high-temperature components in Wild 2 clearly indicate that cycling and long-range transport of material occurred in the early solar system on a massive scale (McKeegan et al. 2006; Nakamura et al. 2008; Oglione et al. 2009; Westphal et al. 2009). This observation is consistent with similar conclusions drawn from isotopic measurements of crystalline silicates in cometary IDPs (Keller and Messenger 2005; Aléon et al. 2009).

Crystalline Silicate Microstructure: Shock and Thermal Histories

While most of the crystalline grains in Stardust samples studied thus far by TEM techniques do not show evidence for shock effects (Zolensky et al. 2006), we identified shock features in the terminal particle of T112, similar to those reported in olivine from other Stardust tracks (Tomeoka et al. 2008). The planar defects in the terminal particle of T112 probably formed during impact into the aerogel collector. Recent experimental work has shown that similar defects develop in olivine from hypervelocity (~ 6 km s $^{-1}$) impacts into aerogel (Stodolna et al. 2010). Experimental impact studies of alumina into forsterite (Lederer et al. 2008) have shown that planar defects in forsteritic olivine develop at velocities as low as approximately 2.8 km s $^{-1}$. Alternatively, the T112 forsterite grain may have experienced this shock event either as a free particle in space during a grain–grain collision, or perhaps while residing in the regolith of Wild 2 during a large collision into the surface of the comet. Collisional processing of cometary materials may have been common in the past. Dynamical simulations and observations of Kuiper Belt objects suggest these objects have undergone significant and ongoing collisional evolution (Davis and Farinella 1997; Brown et al. 2007), and images of 81P/Wild 2

acquired during the Stardust spacecraft flyby show circular topographic features consistent with impact craters (Brownlee et al. 2004).

Enstatite

The T113 enstatite grains are predominantly ortho-enstatite, but contain a few percentages of clino-lamellae. This microstructure is consistent with formation initially at high temperature (> 1200 °C) in the proto-enstatite field and relatively slow cooling, on the order of 10–20 °C h $^{-1}$, based on the cooling rate experiments of Brearley and Jones (1993).

Nepheline

Nepheline is an extremely rare phase in Stardust samples with only two occurrences documented thus far (Keller et al. 2008; Zolensky, personal communication). Nepheline is a rare phase in primitive meteorites and its petrogenesis is generally attributed to Na metasomatism of aluminosilicate glass or crystalline feldspar (Tomeoka and Itoh 2005). In T113, the polycrystalline nepheline occurs interstitial to enstatite and olivine. We interpret this texture as a devitrification product of NaAlSi $_3$ O $_8$ glass. The T113 enstatite and olivine have equilibrated Mg/Mg + Fe ratios, and while olivine and nepheline glass can stably coexist at high temperatures in the Na $_2$ O–Al $_2$ O $_3$ –MgO–SiO $_2$ system, enstatite and nepheline do not. The stable assemblage for this composition in this system is olivine + albite, and their stability fields separate enstatite and nepheline. Nepheline-normative glass is unusual and has been observed only in rare chondrules in ordinary chondrites (Bridges and Hutchison 1995). The association of enstatite + forsterite + nepheline represents a disequilibrium assemblage, with enstatite and forsterite crystallizing at high temperatures from a melt and in equilibrium, yet the residual melt composition suggests that the formation of feldspathic glass was suppressed in favor of nepheline-normative glass. This is similar to the formation conditions proposed for nepheline-bearing mesostasis in a radiating pyroxene chondrule (Bridges and Hutchison 1995). Alternatively, the nepheline-normative glass may represent a high-temperature residue of an initially albite-normative glass that lost SiO $_2$ through evaporation (e.g., Yakovlev et al. 1996).

Origin and Evolution of Cometary Organic Matter

While no organic matter was associated with the terminal particle of track T112, three of the eight terminal particles and an interior section of the main cavity of track T113 did have organic matter with varied

abundances and differing complexities. Our observations suggest that the distribution of organic phases within Wild 2 is heterogeneous in both abundance and diversity down to submicrometer-scale lengths. This suggests that no large scale homogenization processes can have occurred with Wild 2 either during or after accretion. This is consistent with the prevailing view of comets as pristine reservoirs of early solar system materials. These observations also argue against any pervasive terrestrial organic contamination of the aerogel, either prior or subsequent to cometary collection. It is possible that much of the original organic background in the aerogel sublimed during the prolonged exposure to hard vacuum during the mission.

While type B tracks like T113 are relatively common accounting for approximately 33% of all Stardust aerogel impact features (Burchell et al. 2008), T113 has an unusually large number of terminal particle tracks extending out from the base of the bulbous main cavity. It is estimated that <1% of type B tracks have five or more terminal particle tracks (Burchell et al. 2008). By tracing back the trajectories of these terminal particles, we located the point at which the original impactor began to fragment (Fig. 12a). We find that the T113 original impactor did not fragment upon initial impact into the aerogel surface but rather disrupted after it had already penetrated some approximately 180 μm into the aerogel. This observation gives insight into the nature of the impactor and the track formation process. The currently accepted model for the formation of the bulbous cavities characteristic of type B tracks is through the impact of weakly bound aggregates whose component subgrains undergo mechanically driven radial expansion upon impact (Trigo-Rodríguez et al. 2008). In this scenario, the contribution to bulb formation by the gas-phase expansion of shock-heated volatiles is considered on thermodynamic grounds, to have played only a minor secondary role. However, the distribution of terminal particle tracks and abundant organic matter indicate that the T113 bulb may have formed in large part as a result of gas-phase expansion of shock-heated volatiles.

While it is generally accepted that at least a fraction of the captured Wild 2 dust particles contain an indigenous organic component (Sandford et al. 2006; Clemett et al. 2010) understanding the nature and abundance of this material is complicated by the collection process. The rapid dissipation of kinetic energy during impact and deceleration cause both the particle and surrounding aerogel to experience an intense thermal pulse, upwards of 2000 K, for a period of up to several hundred nanoseconds (Roskosz et al. 2008). During this time, thermal alteration and or destruction of organic species present in the impacting particle are

likely to occur. In T113, while the highest concentration of organics is associated with the terminal particles, the bulk abundance of the organic matter (likely >90%) is actually present within and along the aerogel track walls. The track walls also demonstrate the greatest spectral complexity and this may in part be a reflection of a thermal alteration overprint (Clemett et al. 2009, 2010). Nevertheless, the identification of prominent odd mass peaks (e.g., 167, 219, 223, and 267 amu) suggests that Wild 2 aromatics show significant heteroatom incorporation which is ascribed to aromatic nitrile species (Clemett et al. 2010). Interestingly, the presence of N-bearing molecules, abundant high-mass species, and spectral complexity are also observed in CP-IDPs, but rarely in meteorites (Clemett et al. 1993). The presence of organo-nitrogen species is of importance to the abiotic evolution of Mars and Earth since the cleavage of $\text{N}\equiv\text{N}$ necessary for the incorporation of N into organic molecules is kinetically inhibited.

We have observed multiple grains of well-crystallized diamond encapsulated by molten aerogel embedded within compressed aerogel area along the T112. There is a possibility diamond cutters may have been used to taper the walls of the Stardust collector's frame (Cheuvront from Lockheed Martin, personal communication). However, the fact that these diamonds are encased in layers of molten aerogel and are located in the track wall rules out the possibility of terrestrial contamination either as chips of the ultramicrotome diamond knife used during sample preparation or an impurity originally contained in the aerogel cell. Therefore, these diamond grains are possibly genuine cometary samples injected into the aerogel cell along with other Wild 2 materials. The diamond grains we found in the Wild 2 sample are far bigger than presolar nanodiamonds found in carbonaceous chondrites (Lewis et al. 1987). The C and N isotopic compositions of the diamond measured here are also distinct from that of presolar nanodiamonds in carbonaceous chondrites ($\delta^{13}\text{C} = -38\text{‰}$; Swart et al. 1983; $\delta^{15}\text{N} = -330\text{‰}$; Lewis et al. 1983). The C and N isotopic compositions of the Wild 2 diamond are most consistent with formation in the solar system.

CONCLUSIONS

We have demonstrated the ability to ultramicrotome an entire track intact without first compressing the aerogel. This innovation allows us to examine the distribution of fragments along the entire track from the entrance hole all the way to the terminal particle. For Track 112, we observed that the mineralogy of fragments along the track axis was different from that of the terminal particle. The fragments are dominated by

melt particles that result from the interaction of the impacting particle with molten aerogel. We have observed multiple grains of well-crystallized diamond. Organic matter in Track 112 was under detection limit. For Track 113, organic matter is heterogeneously distributed both along aerogel tracks and between terminal particles. These differences in the distribution and abundance of organics suggest that sample contamination via a common source is not responsible for the observed results. Impact shock heating has altered, although not necessarily obscured, the organic inventory of captured cometary grains.

Our most important findings from the analysis of these two Wild 2 aerogel tracks and their terminal particles include:

- The terminal particles in T112 and T113 are dominated by Mg-rich crystalline silicates (forsterite and enstatite) that formed at high temperatures.
- The crystalline silicates have O isotopic within the range of meteoritic materials, implying that they originated in the inner solar system.
- The forsterite grain shows a ^{16}O -enrichment of approximately 40‰, and likely formed in the inner solar system. This grain may have formed together with amoeboid olivine aggregates in meteorites.
- We identified nepheline that formed as a devitrification product of $\text{NaAlSi}_3\text{O}_8$ glass.
- We identified submicrometer diamond grains probably formed in the solar system.
- We identified complex aromatic hydrocarbons distributed along aerogel tracks and in terminal particles. These organics are likely cometary but affected by shock heating.
- We have identified cometary grains contain N-rich organic matter in the form of aromatic nitriles ($\text{R}-\text{C}\equiv\text{N}$). Such materials have potential astrobiological importance as comets are significantly contributed to the prebiotic chemical inventory of both the Earth and Mars.
- The Stardust organic compounds share some similarities with those of carbonaceous chondrites, but are more similar to IDPs. These findings are consistent with the notion that a fraction of interplanetary dust is cometary.

Acknowledgments—The authors thank two anonymous referees whose suggestions helped improve the manuscript. We also thank Dr. Don Brownlee from University of Washington, Allan Chevront and Joseph Vellinga from Lockheed Martin, and Dr. Steven Jones from NASA/JPL for detailed discussion on the Stardust aerogel sample collector fabrication and installation. The Wild 2 samples were provided by the cosmic dust curation facility at NASA Johnson Space Center. The

work was supported by a grant from the NASA LARS program to S. M.

Editorial Handling—Dr. Scott Sandford

REFERENCES

- Aléon J., Engrand C., Leshin L. A., and McKeegan K. D. 2009. Oxygen isotopic composition of chondritic interplanetary dust particles: A genetic link between carbonaceous chondrites and comets. *Geochimica et Cosmochimica Acta* 73:4558–4575.
- Bockelée-Morvan D., Crovisier J., Mumma M. J., and Weaver H. A. 2004. The composition of cometary volatiles. In *Comets II*, edited by Festou M. C., Keller H. U., and Weaver H. A. Tucson, Arizona: The University of Arizona Press. pp. 391–423.
- Bradley J. P. 1994. Chemically anomalous, preaccretionally irradiated grains in interplanetary dust from comets. *Science* 265:925–929.
- Brearley A. J. and Jones R. H. 1993. Chondrite thermal histories from low-Ca pyroxene microstructures: Autometamorphism vs. prograde metamorphism revisited (abstract #185). 24th Lunar and Planetary Science Conference. CD-ROM.
- Bridges J. C. and Hutchison R. 1995. Silica under- and oversaturated mineral assemblages in chondrule mesostases (abstract). *Meteoritics* 30:491.
- Brown M. E., Barkume K. M., Ragozzine D., and Schaller E. L. 2007. A collisional family of icy objects in the Kuiper belt. *Nature* 446:294–296.
- Brownlee D. E., Hörz F., Newburn R. L., Zolensky M. E., Duxbury T. C., Sandford S., Sekanina Z., Tsou P., Hanner M. S., Clark B. C., Green S. F., and Kissel J. 2004. Surface of young Jupiter family comet 81 P/Wild 2: View from the Stardust spacecraft. *Science* 304:1764–1769.
- Brownlee D., Tsou P., Aléon J., Alexander C. M. O' D., Araki T., Bajt S., Baratta G. A., Bastien R., Bland P., Bleuet P., Borg J., Bradley J. P., Brearley A., Brenker F., Brennan S., Bridges J. C., Browning N. D., Brucato J. R., Bullock E., Burchell M. J., Busemann H., Butterworth A., Chaussidon M., Chevront A., Chi M., Cintala M. J., Clark B. C., Clemett S. J., Cody G., Colangeli L., Cooper G., Cordier P., Daghlian C., Dai Z., D'Hendecourt L., Djouadi Z., Dominguez G., Duxbury T., Dworkin J. P., Ebel D. S., Economou T. E., Fakra S., Fairey S. A. J., Fallon S., Ferrini G., Ferroir T., Fleckenstein H., Floss C., Flynn G., Franchi I. A., Fries M., Gainsforth Z., Gallien J.-P., Genge M., Gilles M. K., Gillet Ph., Gilmour J., Glavin D. P., Gounelle M., Grady M. M., Graham G. A., Grant P. G., Green S. F., Grossemy F., Grossman L., Grossman J. N., Guan Y., Hagiya K., Harvey R., Heck P., Herzog G. F., Hoppe P., Hörz F., Huth J., Hutcheon I. D., Ignatyev K., Ishii H., Ito M., Jacob D., Jacobsen C., Jacobsen S., Jones S., Joswiak D., Jurewicz A., Kearsley A. T., Keller L. P., Khodja H., Kilcoyne A. L. D., Kissel J., Krot A., Langenhorst F., Lanzirrotti A., Le L., Leshin L. A., Leitner J., Lemelle L., Leroux H., Liu M.-C., Luening K., Lyon I., MacPherson G., Marcus M. A., Marhas K., Marty B., Matrajt G., McKeegan K., Meibom A., Mennella V., Messenger K., Messenger S., Mikouchi T., Mostefaoui S., Nakamura T., Nakano T., Newville M., Nittler L. R., Ohnishi I., Ohsumi K., Okudaira K., Papanastassiou D. A., Palma R., Palumbo M. E., Pepin R. O., Perkins D.,

- Perronnet M., Pianetta P., Rao W., Rietmeijer F. J. M., Robert F., Rost D., Rotundi A., Ryan R., Sandford S. A., Schwandt C. S., See T. H., Schlutter D., Sheffield-Parker J., Simionovici A., Simon S., Sitnitsky I., Snead C. J., Spencer M. K., Stadermann F. J., Steele A., Stephan T., Stroud R., Susini J., Sutton S. R., Suzuki Y., Taheri M., Taylor S., Teslich N., Tomeoka K., Tomioka N., Toppani A., Trigo-Rodríguez J. M., Troadec D., Tsuchiyama A., Tuzzolino A. J., Tyliczszak T., Uesugi K., Velbel M., Vellenga J., Vicenzi E., Vincze L., Warren J., Weber I., Weisberg M., Westphal A. J., Wirick S., Wooden D., Wopenka B., Wozniakiewicz P., Wright I., Yabuta H., Yano H., Young E. D., Zare R. N., Zega T., Ziegler K., Zimmerman L., Zinner E., and Zolensky M. 2006. Comet 81P/Wild 2 under a microscope. *Science* 314:1711–1716.
- Burchell M. J., Fairey S. A. J., Wozniakiewicz P., Brownlee D. E., Hörz F., Kearsley A. T., See T. H., Tsou P., Westphal A., Green S. F., Trigo-Rodríguez J. M., and Dominguez G. 2008. Characteristics of cometary dust tracks in Stardust aerogel and laboratory calibrations. *Meteoritics & Planetary Science* 43:23–40.
- Clemett S. J., Maechling C. R., Zare R. N., Swan P. D., and Walker R. M. 1993. Identification of complex aromatic molecules in individual interplanetary dust particles. *Science* 262:721–725.
- Clemett S. J., Nakamura-Messenger K., and McKay D. S. 2009. Origin and evolution of organic matter preserved in Stardust cometary aerogel track (abstract #2395). 40th Lunar and Planetary Science Conference. CD-ROM.
- Clemett S. J., Sandford S. A., Nakamura-Messenger K., Hörz F., and McKay D. S. 2010. Complex aromatic hydrocarbons in Stardust samples collected from comet 81P/Wild 2. *Meteoritics & Planetary Science* 45:701–722.
- Cliff G. and Lorimer G. W. 1975. The quantitative analysis of thin specimens. *Journal of Microscopy* 103:203–207.
- Crovisier J., Leech K., Bockelee-Morvan D., Brooke T. Y., Hanner M. S., Altieri B., Keller H. U., and Lellouch E. 1997. The spectrum of comet Hale-Bopp (C/1995 01) observed with the Infrared Space Observatory at 2.9 AU from the Sun. *Science* 275:1904–1907.
- Davis D. R. and Farinella P. 1997. Collisional evolution of Edgeworth-Kuiper belt objects. *Icarus* 125:50–60.
- Fagan T. J., Krot A. N., Keil K., and Yurimoto H. 2004. Oxygen isotopic evolution of amoeboid olivine aggregates in the reduced CV3 chondrites Efremovka, Vigarano, and Leoville. *Geochimica et Cosmochimica Acta* 68:2591–2611.
- Flynn G. J., Bleuet P., Borg J., Bradley J. P., Brenker F. E., Brennan S., Bridges J., Brownlee D. E., Bullock E. S., Burghammer M., Clark B. C., Dai Z. R., Daghlian C. P., Djouadi Z., Fakra S., Ferroir T., Floss C., Franchi I. A., Gainsforth Z., Gallien J.-P., Gillet P., Grant P. G., Graham G. A., Green S. F., Grossemy F., Heck P. R., Herzog G. F., Hoppe P., Hörz F., Huth J., Ignatyev K., Ishii H. A., Janssens K., Joswiak D., Kearsley A. T., Khodja H., Lanzirotti A., Leitner J., Lemelle L., Leroux H., Luening K., MacPherson G. J., Marhas K. K., Marcus M. A., Matrajt G., Nakamura T., Nakamura-Messenger K., Nakano T., Newville M., Papanastassiou D. A., Pianetta P., Rao W., Riekel C., Rietmeijer F. J. M., Rost D., Schwandt C. S., See T. H., Sheffield-Parker J., Simionovici A., Sitnitsky I., Snead C. J., Stadermann F. J., Stephan T., Stroud R. M., Susini J., Suzuki Y., Sutton S. R., Taylor S., Teslich N., Troadec D., Tsou P., Tsuchiyama A., Uesugi K., Vekemans B., Vicenzi E. P., Vincze L., Westphal A. J., Wozniakiewicz P., Zinner E., and Zolensky M. E. 2006. Elemental compositions of comet 81P/Wild 2 samples collected by Stardust. *Science* 314:1731–1735.
- Forster B., Van De Ville D., Berent J., Sage D., and Unser M. 2004. Complex wavelets for extended depth-of-field: A new method for the fusion of multichannel microscopy images. *Microscopy Research and Technique* 65:33–42.
- Grossman L. and Steel I. M. 1976. Amoeboid olivine aggregates in the Allende meteorite. *Geochimica et Cosmochimica Acta* 40:149–155.
- Hanner M. S., Lynch D. K., and Russell R. W. 1994. The 8-13 micron spectra of comets and the composition of silicate grains. *The Astrophysical Journal* 425:274–285.
- Hiyagon H. and Hashimoto A. 1999. ¹⁶O excesses in olivine inclusions in Yamato-86009 and Murchison chondrites and their relation to CAIs. *Science* 283:828–831.
- Hörz F., Bastien R., Borg J., Bradley J. P., Bridges J. C., Brownlee D. E., Burchell M. J., Chi M., Cintala M. J., Dai Z. R., Djouadi Z., Dominguez G., Economou T. E., Fairey S. A. J., Floss C., Franchi I. A., Graham G. A., Green S. F., Heck P., Hoppe P., Huth J., Ishii H., Kearsley A. T., Kissel J., Leitner J., Leroux H., Marhas K., Messenger K., Schwandt C. S., See T. H., Snead C., Stadermann F. J., Stephan T., Stroud R., Teslich N., Trigo-Rodríguez J. M., Tuzzolino A. J., Troadec D., Tsou P., Warren J., Westphal A., Wozniakiewicz P., Wright I., and Zinner E. 2006. Impact features on Stardust: Implications for comet 81P/Wild 2 dust. *Science* 314:1716–1719.
- Ishii H. A., Bradley J. P., Dai Z. R., Chi M., Kearsley A. T., Burchell M. J., Browning N. D., and Molster F. 2008. Comparison of comet 81P/Wild 2 dust with interplanetary dust from comets. *Science* 319:447–450.
- Keller L. P. and Messenger S. 2005. The nature and origin of interplanetary dust: High-temperature components. In *Chondrites and the protoplanetary disk*, edited by Krot A. N., Scott E. R. D., and Reipurth B. *Astronomical Society of the Pacific Conference Series* 341:657–665.
- Keller L. P., Bajt S., Baratta G. A., Borg J., Bradley J. P., Brownlee D. E., Busemann H., Brucato J. R., Burchell M., Colangeli L., D'Hendecourt L., Djouadi Z., Ferrini G., Flynn G., Franchi I. A., Fries M., Grady M. M., Graham G. A., Grossemy F., Kearsley A., Matrajt G., Nakamura-Messenger K., Mennella V., Nittler L., Palumbo M. E., Stadermann F. J., Tsou P., Rotundi A., Sandford S. A., Snead C., Steele A., Wooden D., and Zolensky M. 2006. Infrared spectroscopy of comet 81P/Wild 2 samples returned by Stardust. *Science* 314:1728–1731.
- Keller L. P., Nakamura-Messenger K., and Messenger S. 2008. Mineralogy and chemistry of Stardust samples (abstract #A459). *Geochimica et Cosmochimica Acta* 72.
- Kemper F., Vriend W. J., and Tielens A. G. G. M. 2004. The absence of crystalline silicates in the diffuse interstellar medium. *The Astrophysical Journal* 609:826–837.
- Kobayashi S., Imai H., and Yurimoto H. 2003. New extreme ¹⁶O-rich reservoir in the early solar system. *Geochemical Journal* 37:663–669.
- Krot A. N., McKeegan K. D., Leshin L. A., MacPherson G. J., and Scott E. R. D. 2002. Existence of an ¹⁶O-rich gaseous reservoir in the solar nebula. *Science* 295:1051–1054.

- Lederer S. M., Cintala M. J., Olney R. D., Keller L. P., Nakamura-Messenger K., and Zolensky M. E. 2008. Collisional processing of olivine and pyroxene in cometary dust (abstract #2316). 39th Lunar and Planetary Science Conference. CD-ROM.
- Lewis R. S., Anders E., Wright I. P., Norris S. J., and Pillinger C. T. 1983. Isotopically anomalous nitrogen in primitive meteorites. *Nature* 305:767–771.
- Lewis R. S., Ming T., Wacker J. F., Anders E., and Steel E. 1987. Interstellar diamonds in meteorites. *Nature* 326:160–162.
- Matrajt G. and Brownlee D. E. 2006. Acrylic embedding of Stardust particles encased in aerogel. *Meteoritics & Planetary Science* 41:1715–1720.
- McKeegan K. D., Aléon J., Bradley J., Brownlee D., Busemann H., Butterworth A., Chaussidon M., Fallon S., Floss C., Gilmour J., Gounelle M., Graham G., Guan Y., Heck P. R., Hoppe P., Hutcheon I. D., Huth J., Ishii H., Ito M., Jacobsen S. B., Kearsley A., Leshin L. A., Liu M.-C., Lyon I., Marhas K., Marty B., Matrajt G., Meibom A., Messenger S., Mostefaoui S., Mukhopadhyay S., Nakamura-Messenger K., Nittler L., Palma R., Pepin R. O., Papanastassiou D. A., Robert F., Schlutter D., Snead C. J., Stadermann F. J., Stroud R., Tsou P., Westphal A., Young E. D., Ziegler K., Zimmermann L., and Zinner E. 2006. Isotopic compositions of cometary matter returned by Stardust. *Science* 314:1724–1728.
- Nakamura T., Noguchi T., Tsuchiyama A., Ushikubo T., Kita N. T., Valley J. W., Zolensky M. E., Kakakzu Y., Sakamoto K., Mashio E., Uesugi K., and Nakano T. 2008. Chondrule-like objects in short-period comet 81P/Wild 2. *Science* 321:1664–1667.
- Nakamura T., Noguchi T., Tsuchiyama A., Ushikubo T., Kita N. T., Valley J., WTakahata N., Sano Y., Zolensky M. E., Kakazu Y., Uesugi K., and Nakano T. 2009. Additional evidence for the presence of chondrules in comet 81P/Wild 2 (abstract #5304). *Meteoritics & Planetary Science* 44.
- Ogliore R. C., Westphal A. J., Gainsforth Z., Butterworth A., Fakra S. C., and Marcus M. A. 2009. Nebular mixing constrained by the Stardust samples. *Meteoritics & Planetary Science* 44:1675–1681.
- Roskosz M., Leroux H., and Watson H. C. 2008. Thermal history, partial preservation and sampling bias recorded by Stardust cometary grains during their capture. *Earth and Planetary Science Letters* 273:195–202.
- Sandford S. A., Aléon J., Alexander C. M. O. D., Araki T., Bajt S., Baratta G. A., Borg J., Bradley J. P., Brownlee D. E., Brucato J. R., Burchell M. J., Busemann H., Butterworth A., Clemett S. J., Cody G., Colangeli L., Cooper G., D'Hendecourt L., Djouadi Z., Dworkin J. P., Ferrini G., Fleckenstein H., Flynn G. J., Franchi I. A., Fries M., Gilles M. K., Glavin D. P., Gounelle M., Grossemy F., Jacobsen C., Keller L. P., Kilcoyne A. L. D., Leitner J., Matrajt G., Meibom A., Mennella V., Mostefaoui S., Nittler L. R., Palumbo M. E., Papanastassiou D. A., Robert F., Rotundi A., Snead C. J., Spencer M. K., Stadermann F. J., Steele A., Stephan T., Tsou P., Tyliczszak T., Westphal A. J., Wirick S., Wopenka B., Yabuta H., Zare R. N., and Zolensky M. E. 2006. Organics captured from comet 81P/Wild 2 by the Stardust spacecraft. *Science* 314:1720–1724.
- Stodolna J., Jacob D., Burchell M. J., and Leoux H. 2010. Collect-induced microstructure modifications in Stardust samples: Some experimental evidences (abstract# 1659). 41st Lunar and Planetary Science Conference. CD-ROM.
- Swart P. K., Grady M. M., Pillinger C. T., Lewis R. S., and Anders E. 1983. Interstellar carbon in meteorites. *Science* 220:406–410.
- Tomeoka K. and Itoh D. 2005. Nepheline formation in chondrules in CO3 chondrites: Relationship to parent-body processes (abstract #5080). *Meteoritics & Planetary Science* 40.
- Tomeoka K., Tomioka N., and Ohnishi I. 2008. Silicate minerals and Si-O glass in comet Wild 2 samples: Transmission electron microscopy. *Meteoritics & Planetary Science* 43:273–284.
- Trigo-Rodríguez J. M., Dominguez G., Burchell M. J., Hörz F., and Llorca J. 2008. Bulbous tracks arising from hypervelocity capture in aerogel. *Meteoritics & Planetary Science* 43:75–86.
- Westphal A. J., Snead C., Butterworth A., Graham G. A., Bradley J., Bajt S., Grant P. G., Bench G., Brennan S., and Pianetta P. 2004. Aerogel keystones: Extraction of complete hypervelocity impact events from aerogel collectors. *Meteoritics & Planetary Science* 39:1375–1386.
- Westphal A. J., Fakra S. C., Gainsforth Z., Marcus M. A., Ogliore R. C., and Butterworth A. L. 2009. Mixing fraction of inner solar system material in comet 81P/Wild2. *The Astrophysical Journal* 694:18–28.
- Wood J. 2004. Formation of chondritic refractory inclusions: The astrophysical setting. *Geochimica et Cosmochimica Acta* 68:4007–4021.
- Yakovlev O. I., Dikov Yu P., Gerasimov M. V., Bychkov A. M., and Wlotzka F. 1996. High-temperature vaporization in the albite-orthoclase system (abstract #1466). 27th Lunar and Planetary Science Conference. CD-ROM.
- Zolensky M. E., Zega T. J., Yano H., Wirick S., Westphal A. J., Weisberg M. K., Weber I., Warren J. L., Velbel M. A., Tsuchiyama A., Tsou P., Toppani A., Tomioka N., Tomeoka K., Teslich N., Taheri M., Susini J., Stroud R., Stephan T., Stadermann F. J., Snead C. J., Simon S. B., Simionovici A., See T. H., Robert F., Rietmeijer F. J. M., Rao W., Perronnet M. C., Papanastassiou D. A., Okudaira K., Ohsumi K., Ohnishi I., Nakamura-Messenger K., Nakamura T., Mostefaoui S., Mikouchi T., Meibom A., Matrajt G., Marcus M. A., Leroux H., Lemelle L., Le L., Lanzirrotti A., Langenhorst F., Krot A. N., Keller L. P., Kearsley A. T., Joswiak D., Jacob D., Ishii H., Harvey R., Hagiya K., Grossman L., Grossman J. N., Graham G. A., Gounelle M., Gillet P., Genge M. J., Flynn G., Ferroir T., Fallon S., Ebel D. S., Dai Z. R., Cordier P., Clark B., Chi M., Butterworth A. L., Brownlee D. E., Bridges J. C., Brennan S., Brearley A., Bradley J. P., Bleuet P., Bland P. A., and Bastien R. 2006. Mineralogy and petrology of comet 81P/Wild 2 nucleus samples. *Science* 314:1735–1739.